AIAA JOURNAL
Vol. 32, No. 3, March 1994

Effect of Reynolds Number and Turbulence on Airfoil Aerodynamics at −90-Degree Incidence

Paul M. Stremel*
NASA Ames Research Center, Moffett Field, California 94035

A method has been developed for calculating the viscous flow about airfoils with and without deflected flaps at −90-deg incidence. This method provides for the solution of the unsteady incompressible Navier-Stokes equations by means of an implicit technique. The solution is calculated on a body-fitted computational mesh using a staggered-grid method. The vorticity is defined at the node points, and the velocity components are defined at the mesh-cell sides. The staggered-grid orientation provides for accurate representation of vorticity at the node points and the continuity equation at the mesh-cell centers. The method provides for the noniterative solution of the flowfield and satisfies the continuity equation to machine zero at each time step. The method is evaluated in terms of its ability to predict two-dimensional flow about an airfoil at −90-deg incidence for varying Reynolds number and laminar/turbulent models. The variations of the average loading and surface pressure distribution due to flap deflection, Reynolds number, and laminar or turbulent flow are presented and compared with experimental results. The comparisons indicate that the calculated drag and drag reduction caused by flap deflection and the calculated average surface pressure are in excellent agreement with the measured results at a similar Reynolds number.

Nomenclature

C_d = drag coefficient, based on c
$\bar{C}_d$ = average drag coefficient, based on c
C_l = lift coefficient, based on c
$\bar{C}_l$ = average lift coefficient, based on c
C_p = surface-pressure coefficient
$\bar{C}_p$ = average surface-pressure coefficient
c = airfoil chord length for undeflected flap
h_η, h_ξ = vector lengths in transformed space
p = pressure
Re = Reynolds number, $U_\infty c/\nu$
t = time
U = fluid velocity
u = velocity component in x direction
u_η, u_ξ = transformed velocity components
v = velocity component in y direction
x, y = Cartesian coordinates, nondimensional
α = incidence angle
δ_f = flap deflection
η = coordinate in transformed space
ν = total viscosity (kinematic + eddy)
ξ = coordinate in transformed space
ω = vorticity

Subscript
∞ = value at farfield

Superscript
$'$ = dimensional quantity

Presented as Paper 93-0206 at the AIAA 31st Aerospace Sciences Meeting, Reno NV, Jan. 11–14, 1993; received Jan. 15, 1993; revision received June 25, 1993; accepted for publication July 8, 1993.

*Aerospace Engineer, Rotorcraft Aeromechanics Branch, Full-Scale Aerodynamics Research Division.

Introduction

THE numerical prediction of download, the vertical drag on a rotorcraft during hover, is of considerable importance in the design analysis of rotorcraft. Download limits helicopter performance in hover and is a significant problem in the design of tilt-rotor configurations, where the lifting wing is immersed in the rotor wake. Because the download caused by the rotor wake severely limits the hover performance of tilt-rotor configurations, a method for accurately predicting tilt-rotor download would provide for the design of configurations with improved hover performance.

Limited success in correlating the results of analysis with results obtained from experiment for two-dimensional download has been achieved. In Ref. 1, correlation of the average loading on the XV-15 tilt-rotor aircraft airfoil, with and without a deflected flap, with experimental results was presented. The calculated loading on the airfoil was significantly overpredicted relative to the experimental results. Surface pressure correlations were not included in that reference, except for the zero flap configuration.

Because of the limited ability to predict two-dimensional download, a method was developed to calculate the flow about bluff bodies[2] and was then applied to the two-dimensional download flowfield to evaluate the method and to correlate the results with experiment.[3] In Ref. 3 the flow was calculated for a Reynolds number of 2×10^2 and compared with experimental results for a Reynolds number of 1×10^6. The comparison of the predicted and measured values was shown to be quite good, although the average download was overpredicted. To further evaluate the method, the prediction of flow at high Reynolds numbers and turbulence modeling must be included. Although a flat plate normal to the freestream flow represents bluff body flow and should be insensitive to Reynolds number variations, an airfoil normal to the freestream flow should exhibit some dependence on Reynolds number. This Reynolds number dependence should increase further with flap deflection owing to the variation in the separation point on the airfoil. A turbulent model would also affect the loading on the airfoil owing to its effect on boundary-layer development.

In this paper the method presented in Refs. 2 and 3 is used to calculate the flow about an airfoil at −90-deg incidence. The flow is calculated for Reynolds numbers varying from 1×10^3 to 1×10^6 and for laminar and turbulent models. To

evaluate the method, the predicted results and the results obtained from experiment for an XV-15 airfoil are compared. These comparisons include results for the average airfoil loading and for the average airfoil surface pressure. The outline of previous research is presented first, followed by the development of the governing equations, a description of the numerical method, results, and conclusions.

Previous Research

The application of the velocity/vorticity formulation to incompressible flow problems has increased significantly over the recent past. The velocity/vorticity formulations provided an alternative to the stream function/vorticity formulation with the ability to be extended to three-dimensional analysis. The first applications of the velocity/vorticity formulation modeled the vorticity by using the vorticity transport equation and the velocity by using Poisson equations derived from the definition of vorticity and the conservation of mass.[4] This formulation was quite straightforward but presented a severe limitation: the discrete continuity equation is not satisfied identically.[5]

In the past, the present author was unable to overcome this limitation by any means of discretizing the Poisson equations for the velocity components. This limitation was further demonstrated by the research of Ref. 6 as applied to the momentum equations. In that reference it was pointed out that a staggered grid (one in which the flow variables are positioned at spatially different locations) must be incorporated to accurately model the continuity equation.

This staggered-grid methodology was first applied to the velocity/vorticity formulation in Ref. 7. In addition the solution to the flowfield velocity was obtained by solving the definition of vorticity and the continuity equation in contrast to the derived Poisson equations for the velocity components as before. In Ref. 8 the staggered-grid methodology of Ref.7 was incorporated in a fully coupled implicit technique for internal flows.

In this paper the coupled solution of the flow variables on a staggered grid, including the implicit solution of the vorticity boundary conditions consistent with the interior vorticity and velocity distributions, is computed. The present research also provides for upwind differencing of the convective terms and a turbulent model to model realistic flows about airfoils.

Problem Formulation

The flowfield is modeled by the velocity/vorticity form of the unsteady, incompressible Navier-Stokes equations. The nondimensional governing equations in Cartesian coordinates are written, for the continuity equation,

$$\frac{\partial u}{\partial x}+\frac{\partial v}{\partial y}=0 \tag{1}$$

and for the vorticity transport equation,

$$\frac{\partial \omega}{\partial t}+\frac{\partial(u\omega)}{\partial x}+\frac{\partial(v\omega)}{\partial y}=\nabla^2\omega/Re \tag{2}$$

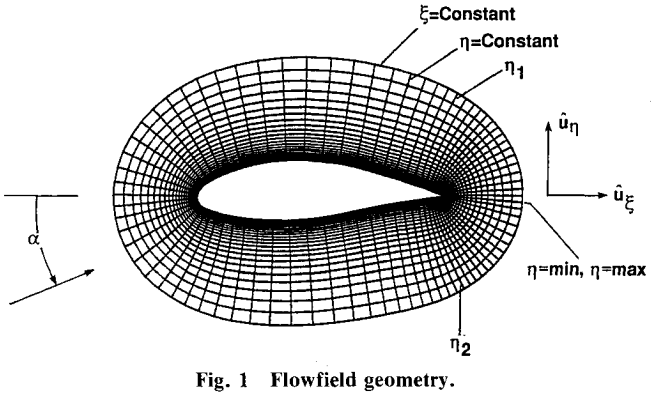

Fig. 1 Flowfield geometry.

with $\nabla^2=\partial^2(\,)/\partial x^2+\partial^2(\,)/\partial y^2$. The vorticity ω is defined by

$$\omega=\frac{\partial v}{\partial x}-\frac{\partial u}{\partial x} \tag{3}$$

The nondimensional variables are written as follows:

$$x=x'/c, \qquad y=y'/c, \qquad u=u'/U_\infty, \qquad v=v'/U_\infty$$

$$\omega=\omega'/(U_\infty/c), \qquad t=t'/(c/U_\infty), \qquad Re=U_\infty c/\nu$$

The turbulent model used in this method is a modified version of the Baldwin and Barth one-equation model.[9,10] This model solves a single advection-diffusion source term equation for the eddy viscosity. The eddy viscosity is added to the kinematic viscosity to obtain the total viscosity for the flow. When laminar flow is considered, the eddy viscosity is set to zero.

A body-fitted computational mesh is used in the finite difference model of the governing equations. A hyperbolic mesh generator was used to generate the computational mesh.[11] A portion of the computational mesh is shown in Fig. 1. The Cartesian equations are transformed into the computational domain (ξ,η), and the governing equations become as follows.

For the continuity equation,

$$[\partial(h_\eta u_\xi)/\partial\xi+\partial(h_\xi u_\eta)/\partial\eta]/(h_\xi h_\eta)=0 \tag{4}$$

for the vorticity transport equation,

$$\partial\omega/\partial t+[\partial(h_\eta u_\xi\omega)/\partial\xi+\partial(h_\xi u_\eta\omega)/\partial\eta]/(h_\xi h_\eta)$$
$$=\{\partial/\partial\xi[(h_\eta/h_\xi)\partial\omega/\partial\xi]+\partial/\partial\eta[(h_\xi/h_\eta)\partial\omega/\partial\eta]\}/(R_e h_\xi h_\eta) \tag{5}$$

and for the definition of vorticity,

$$\omega=[\partial(h_\eta u_\eta)/\partial\xi-\partial(h_\xi u_\xi)/\partial\eta]/(h_\xi h_\eta) \tag{6}$$

where

$$h_\xi=(x_\xi^2+y_\xi^2)^{1/2}, \qquad h_\eta=(x_\eta^2+y_\eta^2)^{1/2}$$

The boundary conditions for the transformed governing equations at the airfoil surface are calculated from the no-slip condition as

$$u_\xi=0, \qquad u_\eta=0 \tag{7}$$

with the vorticity at this location calculated from Eq. (6).

The boundary conditions at the far-field boundary are

$$u_\xi=[x_\xi U_\infty\cos(\alpha)+y_\xi U_\infty\sin(\alpha)]/h\xi \tag{8a}$$

$$u_\eta=[x_\eta U_\infty\cos(\alpha)+y_\eta U_\infty\sin(\alpha)]/h_\eta \tag{8b}$$

$$\omega=0 \tag{9}$$

in the potential flow region upstream of the airfoil, that is, for $\eta_1<\eta<\eta_2$ of Fig. 1, with η increasing in the counterclockwise direction.

In the region downstream of the airfoil, the vorticity at the far-field boundary is calculated from Eq. (5) by considering the inertial terms only and neglecting the viscous terms. Therefore, the vorticity at the far-field boundary, for $\eta_2<\eta<\eta_{\max}$ and for $\eta_{\min}<\eta<\eta_1$, is calculated from

$$\partial\omega/\partial t+[\partial(h_\eta u_\xi\omega)/\partial\xi+\partial(h_\xi u_\eta\omega)/\partial\eta]/(h_\xi h_\eta)=0 \tag{10}$$

using one-sided differencing for $\partial(h_\eta u_\xi\omega)/\partial\xi$.

The flow is started impulsively. An impulsive start requires that the flowfield velocity be equal to the potential flow, except at the airfoil surface, where the velocity is zero, and the initial distribution of surface vorticity is calculated from this potential-velocity field. The boundary condition for the sur-

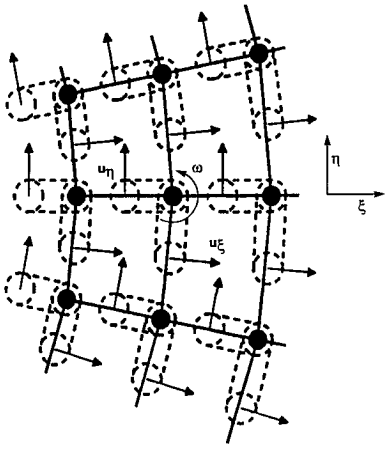

Fig. 2 Schematic for the staggered-grid formulation.

face vorticity after the impulsive start is calculated implicitly as part of the solution. The velocity and vorticity far-field boundary conditions are calculated implicitly as part of the solution from Eqs. (4), (6), and (10).

The computation is advanced until a desired time has been reached or until the flow has demonstrated stable periodic loading on the airfoil. Because of the large gradient of vorticity at the surface of the airfoil at a Reynolds number of 1×10^6, the surface pressure is calculated by an integral method outlined in Ref. 12. This method is accurate for high Reynolds number flows and is consistent with the pressure calculation of Refs. 2 and 3 at low Reynolds numbers. The method was modified for the staggered-grid methodology.

Numerical Method

The solution is obtained by solving the finite difference representations of the governing equations on the body-fitted computational mesh. The grid is finely spaced near the airfoil surface, to resolve the flow, and is more coarsely spaced away from the airfoil, for computational efficiency.

In the staggered-grid method, the flowfield variables are not defined at the mesh nodes only. Rather, the vorticity is defined at the nodes, and the velocity components are defined at the sides of the mesh cells. The vorticity and velocity components on the staggered grid are depicted in Fig. 2.

The vorticity and flowfield velocities are calculated by a fully coupled implicit technique on the staggered mesh. The coupled method solves for the vorticity and velocity components by means of a block-tridiagonal inversion for fractional steps. Each fractional step represents a computational sweep in one of the coordinate directions. The boundary conditions are calculated implicitly as part of the solution. After the inversion of these block-tridiagonal systems, the solution for the present time step is obtained. The solution is not iterated, and the continuity equation is satisfied to machine zero. The solution is then advanced by updating the flowfield variables and solving the flow for the next time step. The solution is terminated at a desired time or after sufficient time has elapsed for demonstration of the flowfield periodicity.

Results

The flow was calculated about an XV-15 tilt-rotor aircraft airfoil (NACA-64A223), with and without a deflected flap, to demonstrate the effects of Reynolds number and laminar/turbulent models on airfoil aerodynamics at $\alpha = -90$ deg. The flowfield Reynolds number was varied from 1×10^3 to 1×10^6, and both laminar and turbulent models were considered in the analysis. The eddy viscosity was calculated using the Baldwin and Barth one-equation model. The airfoil coordinates for the XV-15 were acquired from Ref. 13. The computational grid is dimensioned 101×131 and extends to 30 chord lengths from the airfoil. A representative grid used in the computations is shown in Fig. 3. The wall normal spacing was set to $0.00005c$ at the largest Reynolds numbers considered. The flow was calculated for the airfoil geometry without flap deflection and for flap deflections of 30, 45, 60, 75, and 90 deg. The flap-hinge point is equal to $x = 0.75$ and $y = 0.02$ for the XV-15 airfoil. The flap-hinge location was obtained from the cited literature, and no attempts were made to determine the minimum value of download achievable by varying the flap-hinge location.

In this section, the time-dependent and average loading, as well as the variation in the surface pressure distribution owing to flap deflection, are presented. Comparisons between the predicted averaged loading and that obtained from experiment are presented. Comparisons of the average airfoil loading and the average surface pressures are included.

Time-Dependent Loading

The time-dependent loadings on the XV-15 airfoil for flap deflections of $\delta_f = 0$ and 60 deg are shown in Fig. 4. The results are shown for a Reynolds number of 1×10^6 while modeling the turbulent flow. These results are shown to demonstrate the time dependence of the flow and the convergence of the average loading on the airfoil. For the geometry with an undeflected flap, the average loading is converged for $t > 80$, whereas the average loading on the airfoil with the flap deflected to $\delta_f = 60$ deg converges for $t > 20$. The load-

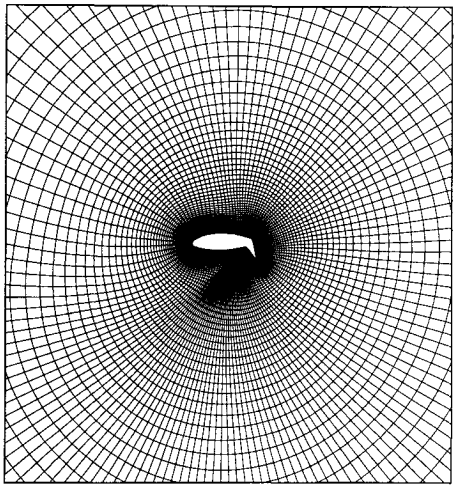

Fig. 3 Typical computational geometry.

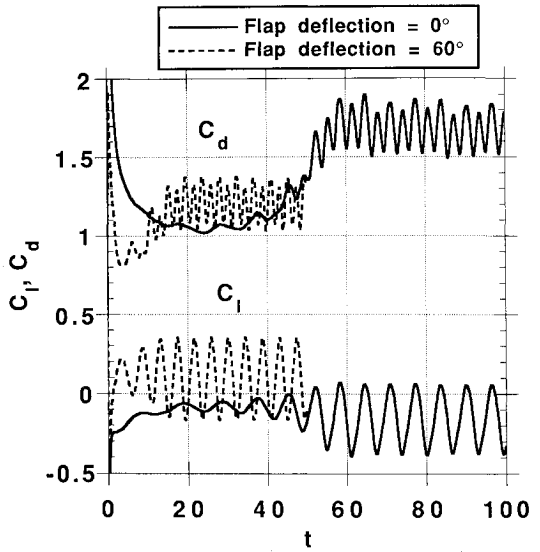

Fig. 4 Time-dependent lift and drag coefficients: $Re = 1 \times 10^6$ and $\alpha = -90$ deg.

ing on the airfoil with the deflected flap quickly converges to a mean lift and drag with oscillations about the mean representative of vortex shedding. The loading for the airfoil with an undeflected flap is somewhat different in that the mean drag does not quickly converge to a steady value. This additional time required for steady-state convergence is the time required for the shed wake to reach stable periodic shedding. The unsteady loadings on the airfoil for the other flap deflections are similar to those shown for $\delta_f = 60$ deg and quickly converge to a mean value.

Average Loading

The average loading for the XV-15 airfoil was calculated by averaging the unsteady loading over several cycles of vortex shedding for a value of time t sufficiently large to eliminate the effects of the impulsive start and insure an invariant average loading. A comparison of the calculated average airfoil loading with the experimental results of Ref. 13 is shown in Figs. 5 and 6. In Fig. 5, a comparison of the predicted average lift and drag for varying Reynolds number with experimental values is presented. The laminar model was used for each prediction to demonstrate the effect of Reynolds number on lift and drag. The experimental results were measured for a freestream Reynolds number of 1×10^6. The drag is overpredicted for all flap deflections and all Reynolds numbers considered (Fig. 5). For no flap deflection, the variation in the predicted drag with Reynolds number is as expected: a decrease in drag for increased Reynolds number. At a Reynolds number of 1×10^6 the predicted drag is only slightly overpredicted when compared with the experimental results. The lift is accurately predicted for all of the Reynolds numbers considered for $\delta_f = 0$ deg.

As the flap deflection is increased, the predicted drag agrees less favorably with the experimental results and at the larger flap deflections, $\delta_f = 60$ and 75 deg, is overpredicted by as much as 25% for the Reynolds numbers considered. A slight improvement in the correlation is shown for increasing Reynolds number. The predicted lift, Fig. 5, closely matches the experimental data up to a flap defection of $\delta_f = 45$ deg, after which the predicted lift is not in close agreement with the experimental data.

The predicted lift and drag for a Reynolds number of 1×10^6 and using the turbulent model are shown in Fig. 6. Shown in the figure, for comparison, are the predicted results for the laminar model and the experimental results. As shown in the figure, the predicted drag for the turbulent model is in

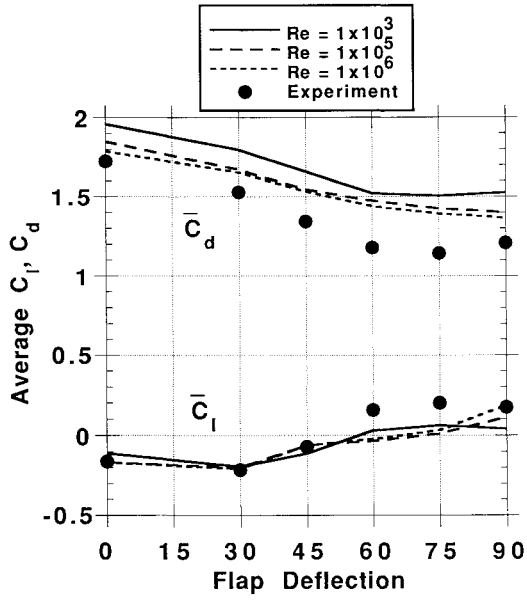

Fig. 5 Comparison of predicted average airfoil lift and drag with experimental values: Reynolds number variation, laminar model, $\alpha = -90$ deg.

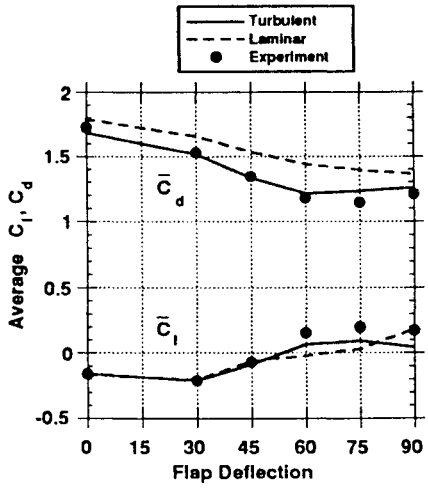

Fig. 6 Comparison of predicted average airfoil lift and drag with experimental values: $Re = 1 \times 10^6$, laminar and turbulent models, $\alpha = -90$ deg.

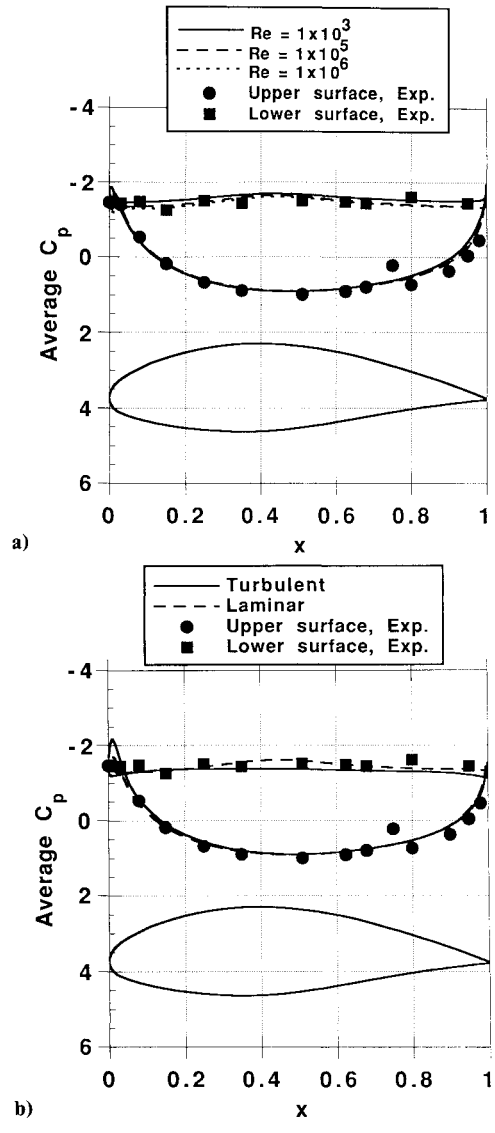

Fig. 7 Comparison of predicted average surface pressure coefficient with experiment, $\alpha = -90$ deg and $\delta_f = 0$ deg: a) Reynolds number variation, laminar model and b) $Re = 1 \times 10^6$, laminar and turbulent models.

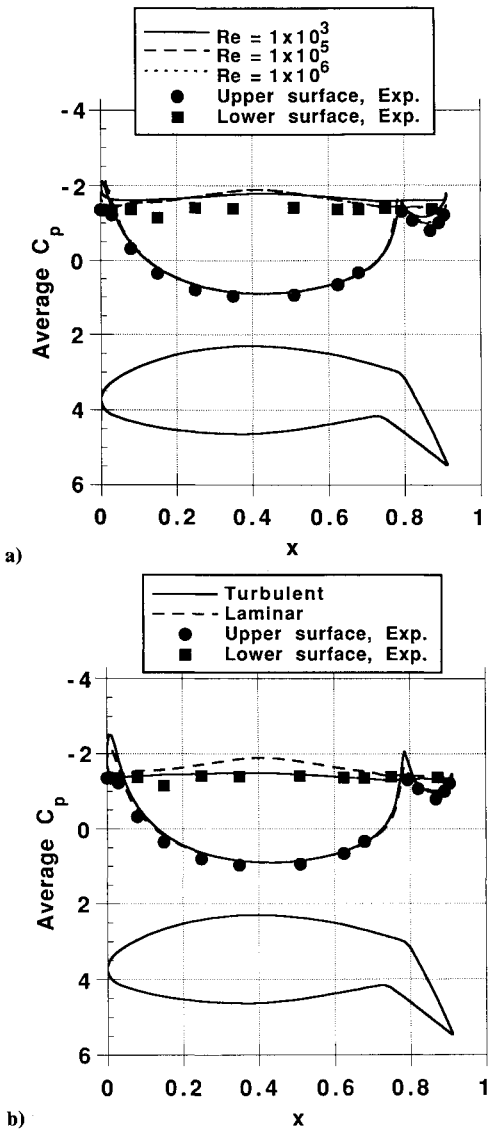

Fig. 8 Comparison of predicted average surface pressure coefficient with experiment, $\alpha = -90$ deg and $\delta_f = 45$ deg: a) Reynolds number variation, laminar model and b) $Re = 1 \times 10^6$, laminar and turbulent models.

excellent agreement with the experimental result and represents a significant improvement in the experimental correlation when compared with the predicted drag using the laminar model. A similar trend is shown for the predicted lift.

Average Surface Pressure Distribution

Comparisons of the calculated pressure distribution and the pressure measured in experiment on the XV-15 airfoil are shown in Figs. 7–10 and are presented for flap deflections of $\delta_f = 0$, 45, 60, and 75 deg, respectively. Experimental data are not available for $\delta_f = 30$ and 90 deg. Each figure presents a comparison of the predicted results for varying Reynolds number while modeling a laminar flow (part a) and a comparison of the predicted surface pressure at a Reynolds number of 1×10^6 for the laminar and turbulent models (part b). Comparisons with experimental data are shown in each figure. Please note that the experimental pressure data of Ref. 13, as presented here, were corrected by the author, because the data were incorrectly plotted in that report and did not accurately reflect the pressure port location due to flap deflection. The corrected data are as yet unpublished.

The pressure distribution for the undeflected flap geometry is shown in Fig. 7. Only small variations in the predicted base pressure (the pressure on the lower surface of the airfoil) due to Reynolds number can be seen (Fig. 7a). This trend is consistent with the small variations in the predicted lift and drag, as shown in Fig. 5, for this geometry. The comparison of the predicted pressure distributions for the laminar and turbulent models is shown in Fig. 7b. Only small variations between the results can be seen. The variations represent a "flattening" of the base pressure and a leading-edge suction peak on the upper surface of the airfoil due to the turbulent model. The experimental data do not show the presence of a leading-edge suction peak.

The pressure distribution for a flap deflection of $\delta_f = 45$ deg is shown in Fig. 8. The variation in the predicted surface pressure for varying Reynolds numbers is shown in Fig. 8a. The variations in the predicted surface pressure are confined mainly to the lower surface of the airfoil and near the leading and trailing edges of the airfoil. This is due to the variation in convection and diffusion of the separated vorticity at the leading and trailing edges of the airfoil owing to Reynolds number variation. The suction peak is again on the upper surface of the airfoil near the leading edge but is insensitive to Reynolds number. In Fig. 8b, the base pressure using the turbulent model is "flattened" with respect to the results for

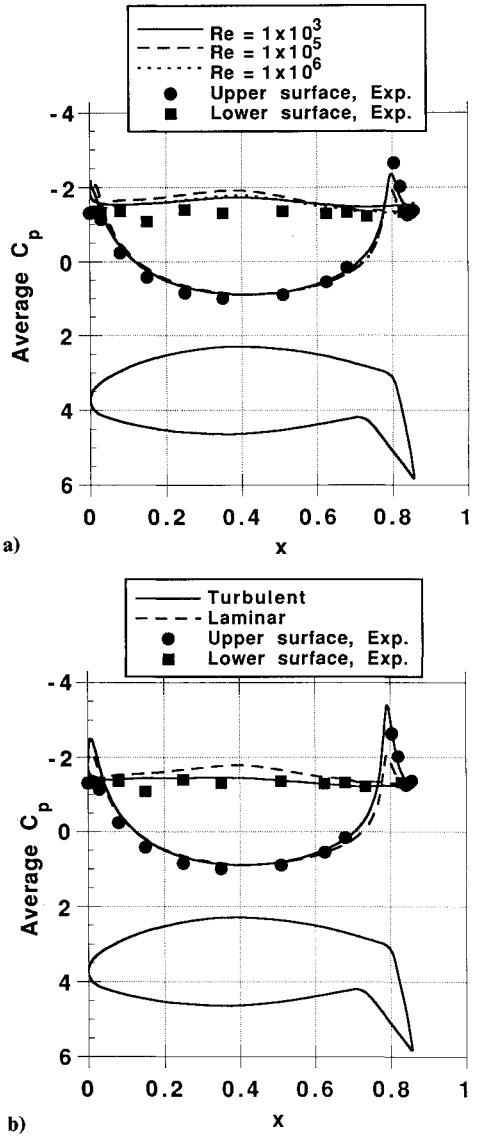

Fig. 9 Comparison of predicted average surface pressure coefficient with experiment, $\alpha = -90$ deg and $\delta_f = 60$ deg: a) Reynolds number variation, laminar model and b) $Re = 1 \times 10^6$, laminar and turbulent models.

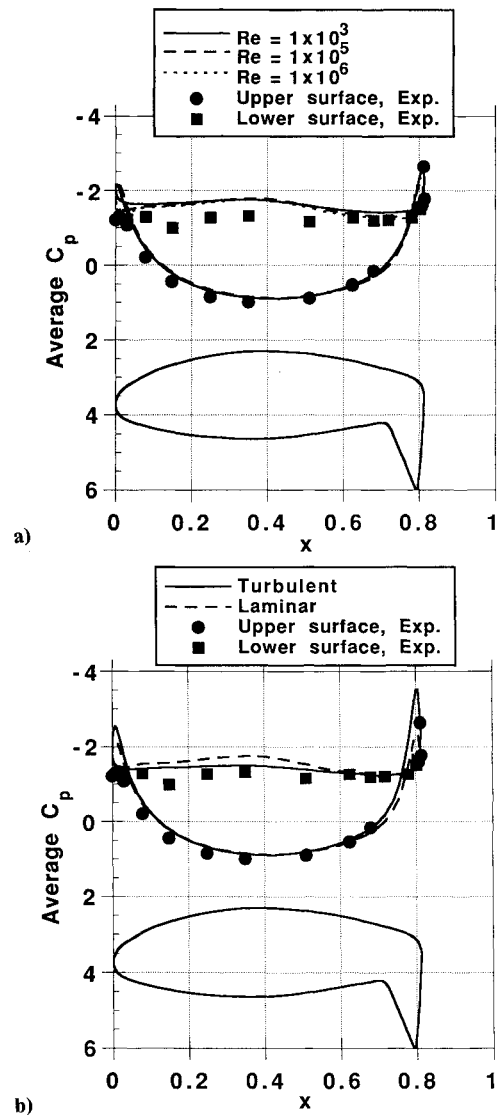

Fig. 10 Comparison of predicted average surface pressure coefficient with experiment, $\alpha = -90$ deg and $\delta_f = 75$ deg: a) Reynolds number variation, laminar model and b) $Re = 1 \times 10^6$, laminar and turbulent models.

the laminar model. This is because the turbulent model provides a more accurate representation of the vorticity diffusion in the wake of the airfoil and hence a more accurate base pressure prediction. In addition, the results for the turbulent model demonstrate an increase in the suction peaks on the upper surface at the leading edge and at the flap-hinge location and are representative of the effects of a turbulent model at these locations.

At a flap deflection of $\delta_f = 60$ deg (Fig. 9), similar results to those for $\delta_f = 45$ deg (Fig. 8) can be seen. Again, the variation in the predicted surface pressure for varying Reynolds numbers is shown to be small and confined mainly to the lower surface of the airfoil and near the leading and trailing edges of the airfoil. In Fig. 9b, the predicted base pressure using the turbulent model is in better correlation with the experimental values when compared with the results using the laminar model. In addition, the results for the turbulent model demonstrate a significant increase in the suction peak on the upper surface at the flap-hinge location when compared with the laminar results. This decrease in the pressure is shown from $x = 0.7$ to the trailing edge of the airfoil and represents a significant improvement in the correlation with the experimental data.

The predicted pressure distribution for $\delta_f = 75$ deg is shown in Fig. 10. These results are very similar to those for $\delta_f = 60$ deg. The results demonstrate a limited variation in the predicted surface pressure owing to Reynolds number variation and a significant improvement in the surface pressure prediction when considering the turbulent model.

Conclusions

A method has been used to predict the viscous flow about an airfoil with and without a deflected flap at an angle of incidence of −90 deg to determine the effect of Reynolds number and laminar/turbulent models on the airfoil loading and surface pressure.

Comparisons of the calculated results with those measured in experiment indicate that the current method accurately predicts the lift and drag on the XV-15 tilt-rotor aircraft airfoil at a Reynolds number of 1×10^6, which is identical to that of the experiment, while using the Baldwin and Barth turbulent boundary-layer model. This was found at all flap deflections from $\delta_f = 0$–90 deg.

The effect of the turbulent model was found to be significant at a Reynolds number of 1×10^6. The drag using a laminar flow model was significantly overpredicted when compared with the experimental results and the results for the turbulent flow model. This was most prevalent at flap deflections between $\delta_f = 45$ and 75 deg and is due to the differences in the prediction of upper surface flow separation and the convection and diffusion of the vorticity in the wake of the airfoil. The variation in the flow separation was clearly demonstrated in the surface pressure distribution comparisons.

The effect of Reynolds number on the predicted results was found to be small when using the laminar flow model. Again, these variations were shown to be most significant at the intermediate flap deflections where the prediction of flow separation is highly dependent on the Reynolds number. This was demonstrated in the airfoil loading and the surface pressure comparisons.

References

[1]Raghavan, V., McCroskey, W. J., Van Dalsem, W. R., and Baeder, J. D., "Calculations of the Flow Past Bluff Bodies, Including Tilt-Rotor Wing Sections at $\alpha = -90°$," AIAA Paper 90-0032, Reno, NV, Jan. 1990.

[2]Stremel, P. M., "Calculation of Flow about Two-Dimensional Bodies by Means of the Velocity-Vorticity Formulation on a Staggered Grid," AIAA Paper 91-0600, Reno, NV, Jan. 1991.

[3]Stremel, P. M., "Calculation of Unsteady Airfoil Loads with and without Flap Deflection at −90 Degrees Incidence," AIAA Paper 91-3336, Baltimore, MD, Sept. 1991.

[4]Fasel, H., "Investigation of the Stability of Boundary Layers by a Finite-Difference Model of the Navier-Stokes Equations," *Journal of Fluid Mechanics,* Vol. 78, Pt. 2, 1976, pp. 355–383.

[5]Roache P. J., *Computational Fluid Dynamics,* 2nd ed., Hermosa Publishers, Albuquerque, NM, 1976, p. 207.

[6]Patankar, S. V., and Spalding, D. B., *Heat and Mass Transfer in Boundary Layers,* 2nd ed., Intertext Books, London, UK, 1970.

[7]Gatski, T. P., Grosch, M. E., and Rose, M. E., "A Numerical Study of the Two-Dimensional Navier-Stokes Equations in Vorticity-Velocity Variables," *Journal of Computational Physics,* Vol. 48, No. 1, 1982, pp. 1–22.

[8]Orlandi, P., "Vorticity-Velocity Formulation for High Re Flows," *Computers and Fluids,* Vol. 15, No. 2, 1987, pp. 137–149,

[9]Baldwin, B. S., and Barth, T. J., "A One-Equation Turbulent Transport Model for High Reynolds Number Wall Bounded Flows," NASA TM-102847, Aug. 1990.

[10]Barth, T. J., "Numerical Aspects of Computing Viscous High Reynolds Number Flow on Unstructured Meshes," AIAA Paper 91-0721, Reno, NV, Jan. 1991.

[11]Cordova, J. Q., and Barth, T. J., "Grid Generation for General 2-D Regions Using Hyperbolic Equations," AIAA Paper 88-0520, Reno, NV, Jan. 1988.

[12]Wang, C. M., Wu, J. C., and Tuncer, I. H., "Accurate Determination of Surface Pressure in High Reynolds Number Flows," First International Conference on Computational Methods in Flow Analysis, Okayama, Japan, Sept. 1988.

[13]Maisel, M. D., Laub, G. H., and McCroskey, W.J., "Aerodynamic Characteristics of Two-Dimensional Wing Configurations at Angles of Attack Near −90 Degrees," NASA TM-88373, Dec. 1986.